RESEARCH ARTICLE

A Wideband Beam Steering and Beamwidth Reconfigurable Antenna Using Coding Metasurface

GANDHAM V. VINOD, (Student Member, IEEE), AND VIKAS V. KHAIRNAR, (Member, IEEE)
School of Electronics Engineering, VIT-AP University, Amaravati, Andhra Pradesh 522237, India

Corresponding author: Vikas V. Khairnar (vikas.vishnu@vitap.ac.in)

ABSTRACT This paper presents a wideband beam steering and beamwidth reconfigurable antenna operating at a center frequency of 3.5 GHz. The proposed antenna consists of a cross-slot serving as the source element, a 19×19 artificial magnetic conductor (AMC) acting as a reflector, and a 9×9 transmissive coding metasurface (TCMS) functioning as a phase gradient. The cross-slot antenna offers a wide bandwidth and produces a bidirectional radiation pattern. Incorporating a 19×19 AMC beneath the source antenna achieves a high gain unidirectional radiation pattern. Additionally, positioning a 9×9 TCMS above the source antenna enables control over the antenna radiation characteristics. The TCMS comprises individual unit cells integrated with PIN diodes. By controlling operating states of the PIN diodes, the proposed antenna achieves beam steering and beamwidth reconfigurability in the yz-plane. Main beam of the antenna is steered from $-57°$ to $+57°$. The proposed antenna offers flexibility in beamwidth reconfiguration, operating in wide beam and narrow beam mode. In wide beam mode, the antenna exhibits a 3-dB beamwidth of $140°$ providing broader coverage. Conversely, in narrow beam mode the 3-dB beamwidth narrows to $60°$ resulting in a more focused radiation pattern. The overall impedance bandwidth of the antenna ranges from 3.09 to 3.70 GHz (17.96%) with peak gain ranging from 5.8 dBi to 8.47 dBi. The simulated and measured results of the proposed antenna are found to be in good agreement.

INDEX TERMS Cross-slot, artificial magnetic conductor (AMC), transmissive coding metasurface (TCMS), beam steering and beamwidth reconfigurability.

I. INTRODUCTION

Future wireless communication applications require reconfigurable antennas to overcome the limitations of conventional antennas. Reconfigurable antennas offer multiple benefits compared to conventional antennas. They allow dynamic adjustments of operational parameters such as frequency, radiation pattern, and polarization. The reconfigurable antennas enable greater flexibility and adaptability in meeting the evolving demands of modern wireless communication technologies [1], [2].

Pattern reconfigurable antenna designs can be categorized into three main types: 1-D beam steering [3], [4], [5], 2-D

beam steering [6], [7], [8], and beamwidth reconfigurability [9], [10], [11]. The majority of beamwidth reconfigurable antenna designs exhibit unidirectional radiation characteristics. It is noted that numerous pattern reconfigurable antenna designs are successful in achieving significant variations in the radiation pattern. Furthermore, several beamwidth reconfigurable antenna designs are reported to achieve 3-dB beamwidth variations in both the principal planes. However, very few antenna designs are reported realizing pattern reconfiguration in terms of both beam steering and beamwidth reconfigurability within a single antenna structure [12], [13], [14], [15], [16], [17], [18], [19], [20], [21]. In this context, the term single antenna structure refers to achieving both beam steering and beamwidth reconfigurability within one antenna. These antennas utilize

---

The associate editor coordinating the review of this manuscript and approving it for publication was Sudipta Chattopadhyay.

various techniques such as parasitic pixel layers [12], tunable parasitic elements [13], [14], [15], partially reflecting surfaces (PRS) [16], antennas with metal walls [17], circular patches [18], and metasurfaces [19], [20], [21].

The antenna design presented in [12] utilizes parasitic pixel layers to enable beam steering and beamwidth reconfigurability at an operating frequency 5 GHz. This antenna realizes beam steering of ±40° with an operating bandwidth of 4%. In [13], four tunable parasitic elements are arranged in cross configuration to achieve continuous beam scanning across the entire azimuthal plane. Furthermore, this antenna offers tunable beamwidth in the *xz*-plane and *yz*-plane. However, overall bandwidth of this antenna is limited to 1.63%. A pattern reconfigurable antenna described in [14] enables beam steering along the *yz*-plane from −20° to +20° and beamwidth tuning from 60° to 130°. In [15], a Yagi-Uda patch antenna design with three layers is utilized to achieve single wide beam and three narrow beams with beam steering from −17° to +14°. The parasitic antenna designs operating on the microstrip Yagi principles offer advantages such as simple design, low cost, and ease of operation. However, they typically have limited beam steering capabilities and narrow operating bandwidth [13].

A reconfigurable PRS antenna proposed in [16] achieves independent beam scanning and dynamic control of beamwidth by integrating varactor diodes. The variation in the 3-dB beamwidth is measured to be 18.7° and 22.4°. Additionally, to stimulate the Fabry-Perot cavity, a phased array in the *yz*-plane is utilized, allowing for beam steering of ±10°. The antennas maximum bandwidth is around 3%. The antenna design presented in [17] demonstrates the capability to switch between six different radiation modes, including narrow beam, wide beam, and four-direction beam modes. In [18], a pattern reconfigurable antenna consisting of circular patches with vertical slots is introduced. At 2.08 GHz, the radiation pattern changes as the beams are turned orthogonally, resulting in a beamwidth ranging from 82° to 190° along the elevation plane and 181° to 91° along the azimuth plane. However, overall impedance bandwidths of these designs are limited.

In [19], a leaky wave antenna operating at 3.3 GHz is introduced utilizing metamaterials to steer main beam from −49° to 50°. Along the *xz*-plane, the beamwidth varies between 37° and 48° with a peak gain of 18 dBi. In [20], a quasi-duplex active integrated antenna is presented operating within the 2.4 GHz frequency range. This antenna can steer its beam from −39° to +36° with the beamwidth varying from 111° to 32° along the E-plane. The overall bandwidth is 20.4% and a maximum gain of 14.5 dBi. These antennas offer high gain, but their beam steering angles are relatively low, and they have a high profile.

The concept of digital coding metamaterials introduced in [22] presents a unit cell of metasurface that can be digitally manipulated to modify electromagnetic waves and unlock various functionalities. This innovative approach enables significant enhancements in antenna performance,

contributing to the substantial growth and progress in the development of 2-D digital metamaterials. The antenna design discussed in [21] explores the utilization of digital coding metasurface based antennas for wide angle beam steering. A three element parasitic antenna with a 7×7 digital coding metasurface is employed to achieve improved beam steering capabilities in the *yz*-plane. By altering operating conditions of the PIN diodes within the unit cell, the antennas transmission characteristics can be controlled. The antenna demonstrates discrete beam steering capabilities of ±85°. The 3-dB beamwidth measures 130° in wide beam mode and 53° in narrow beam mode. However, overall bandwidth remains limited to 0.7% across all operating states. From the literature, it is noted that very few antenna designs are able to achieve both independent beam steering and beamwidth reconfigurability within a single antenna structure. Furthermore, the majority of reported antenna designs are capable of realizing pattern reconfiguration over a narrow operating bandwidth. The objective of this work is to develop a wideband reconfigurable antenna that can provide independent wide angle beam steering and beamwidth reconfigurability.

This paper presents a coding metasurface based wideband reconfigurable antenna capable of achieving beam steering and beamwidth reconfiguration. The proposed antenna utilizes a basic cross-slot backed with an artificial magnetic conductor (AMC). By integrating PIN diodes with a transmissive coding metasurface (TCMS), the antenna achieves different transmissive responses for the *x*-polarized wave. The antenna offers a scanning range of ±57°, with a gain ranging between 5.8 dBi and 8.47 dBi, and an overall impedance bandwidth of 3.09 to 3.70 GHz (17.96%). Additionally, the antenna has capability to switch between wide beam and narrow beam operating mode. Remaining sections of the paper are organized as follows: Section II discusses geometrical design of the cross-slot, AMC, and TCMS. Section III presents working principle of the proposed antenna. In Section IV detailed simulated and measured results are presented. Finally, Section V provides concluding remarks.

II. ANTENNA DESIGN

Fig. 1 illustrates a cross-sectional view of the proposed antenna. It consists of a cross-slot antenna on substrate 1, an AMC on substrate 2, and TCMS as the superstrate on substrate 3. The antenna is designed using an FR4 substrate with a dielectric constant of $\epsilon_r = 4.5$ and a loss tangent of $\tan \delta = 0.02$. The thickness of substrate 1 is 0.8 mm, whereas the thickness of substrate 2 and substrate 3 is 1.6 mm. Full-wave simulation of the proposed antenna is completed using Ansys HFSS [23]. The separation between substrate 1 and substrate 2 is denoted by h_1, while the separation between substrate 1 and substrate 3 is represented by h_2.

A. CROSS-SLOT ANTENNA

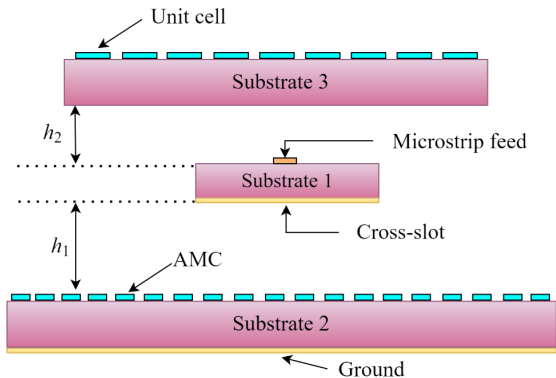In the proposed antenna design, a cross-slot is employed as the main radiating element placed on the lower side of

FIGURE 1. Cross-sectional view of the proposed antenna.

substrate 1. To reduce the occupied space of the main radiator, cross-slot is placed at a 45° angle with respect to the axis line. The microstrip feed is positioned on the top side of substrate 1. To achieve wideband performance, the radiating slot is designed with an electrical length of approximately $0.5\lambda_g$. Geometrical design of cross-slot antenna and microstrip feed line is shown in Fig. 2. Optimized dimensions of the cross-slot are as follows (in mm): substrate length $l = 28$ and substrate width $w = 28$, length of the cross-slot $l_1 = 26.13$, and width of the cross-slot $w_1 = 3$. In order to achieve wideband impedance matching, the cross-slot antenna employs a stepped microstrip feed line. Optimized dimensions of the microstrip feed line are as follows (in mm): $l_2 = 15.5$, $l_3 = 6.6$, $l_4 = 3$, $l_5 = 1.5$, $w_2 = 1.5$, $w_3 = 0.7$, $w_4 = 0.4$, and $w_5 = 0.4$. The cross-slot antenna achieves an impedance bandwidth of 3.09 to 4.54 GHz (1.44 GHz, 37.74%), as shown in Fig. 3(a). Normalized radiation patterns along the xz-plane and yz-plane are depicted in Fig. 3(b) and Fig. 3(c), respectively. In the xz-plane, the antenna displays a bidirectional radiation pattern, while in the yz-plane, it exhibits an omnidirectional radiation pattern. The maximum gain attained by the cross-slot antenna is 3.35 dBi.

B. ARTIFICIAL MAGNETIC CONDUCTOR (AMC)

An AMC is similar to a perfect electrical conductor (PEC), but exhibits a zero reflection phase as opposed to the conventional 180° reflection phase. The cross-slot antenna emits radiation in two directions, specifically along the $+z$-axis and $-z$-axis. To achieve unidirectional radiation characteristics, an AMC is positioned beneath the cross-slot antenna. This configuration effectively reduces backward radiation and enables the antenna to predominantly emit the beam in forward direction. Geometrical design of the AMC unit cell is illustrated in Fig. 4(a). It consists of a square-shaped unit cell with a length of $l_6 = 7$ mm and a periodicity of $p_1 = 7.7$ mm. The substrate is accompanied by a ground plane positioned beneath it forming the same boundary as the substrate. The AMC exhibits an operating bandwidth of 2.68 to 4.26 GHz (1.57 GHz, 45.31%) in terms of the ±45° reflection phase, as depicted in Fig. 4(b).
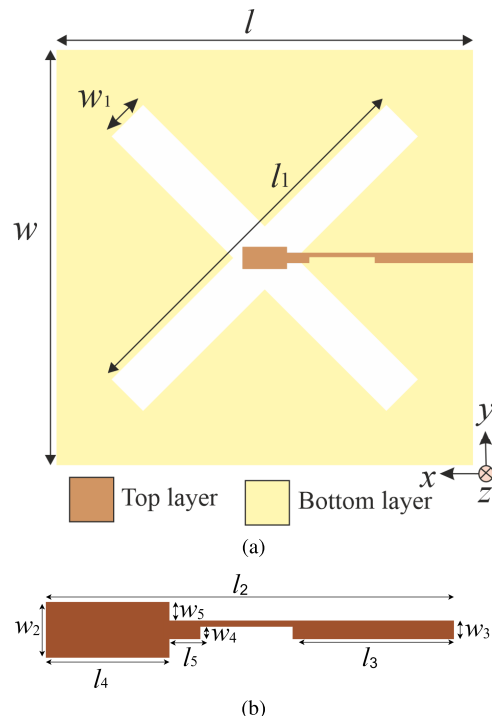

FIGURE 2. Geometrical design of (a) Cross-slot antenna and (b) Microstrip feed line.
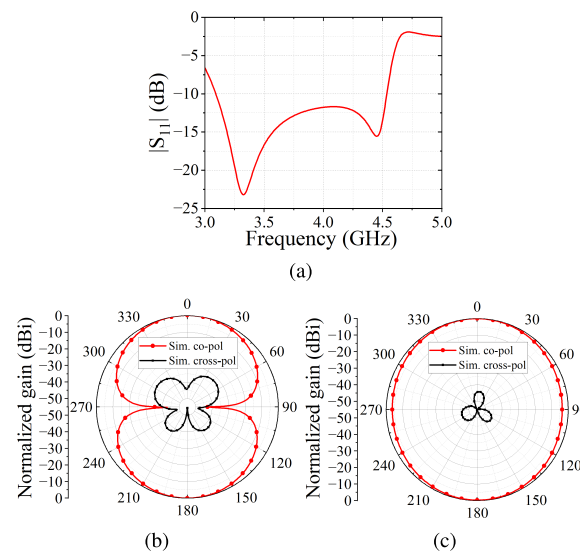

FIGURE 3. Simulated results of the cross-slot antenna (a) Reflection characteristics, (b) Normalized radiation pattern in the *xz*-plane at 3.5 GHz, and (c) Normalized radiation pattern in the *yz*-plane at 3.5 GHz.

In the proposed design AMC surface comprises of 19×19 periodic patch unit cells and is positioned beneath the source antenna at a distance of $h_1 = 21.4$ mm ($\approx 0.25\lambda_0$) [24]. The reflection characteristics of the cross-slot antenna with the AMC exhibit an operating bandwidth from 3 to 4.52 GHz (1.50 GHz, 39.89%), as shown in Fig. 5(a). The simulated normalized radiation patterns of the cross-slot antenna with the AMC in xz-plane and yz-plane, are depicted in Fig. 5(b) and Fig. 5(c), respectively. This arrangement leads to the
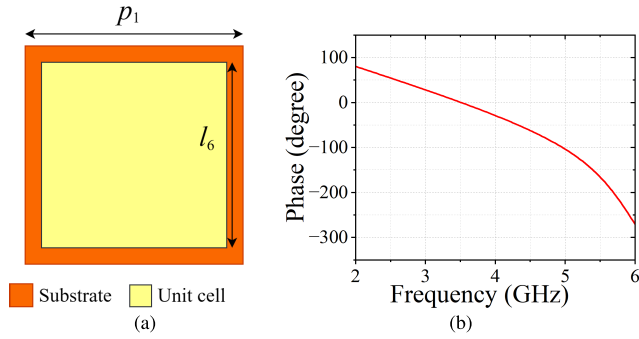
FIGURE 4. (a) Geometrical design of the AMC unit cell and (b) Reflection phase characteristics exhibited by the AMC.

cross-slot antenna exhibiting directional radiation properties with a maximum gain of 7.11 dBi. The cross-polarization level is observed to be less than -35 dB in both planes. The integration of an AMC with the cross-slot antenna enhances overall gain of the antenna.
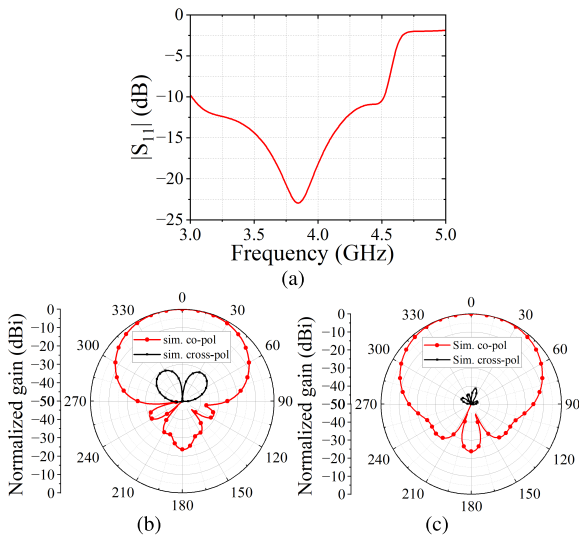

FIGURE 5. Simulated results of the cross-slot antenna with AMC (a) Reflection characteristics, (b) Normalized radiation pattern along the *xz*-plane at 3.5 GHz, and (c) Normalized radiation pattern along the *yz*-plane at 3.5 GHz.

C. TRANSMISSIVE CODING METASURFACE (TCMS)

This section presents a comprehensive discussion about TCMS design. The proposed TCMS design comprises a 9×9 array of unit cells. The metasurface layer is composed of sub-wavelength unit cells that are simple and symmetric, serving as transmissive units. Geometrical design of the proposed unit cell is depicted in Fig. 6(a). Optimized dimensions of the unit cell are as follows (in mm): $p = 16$, $v = 13$, $k = 5$, $a = 1.6$, $b = 0.6$, $c = 5$, $d = 1$, $x = 0.55$, and $y = 2.4$. Performance of the proposed unit cell is characterized in Ansys HFSS using Floquet port boundary conditions. The simulated model used in HFSS is shown in Fig. 6(b). Magnitude and phase characteristics are obtained by considering a de-embedding distance of 30.4 mm ($\approx \lambda/4$).

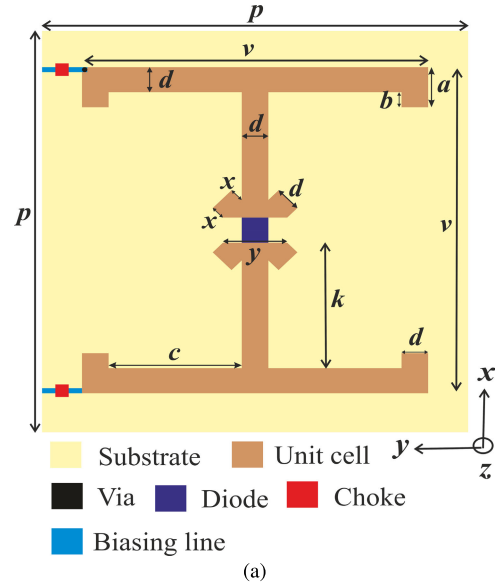The proposed unit cell structure can be envisioned as an improved schematic of an electric inductive-capacitive (ELC)

FIGURE 6. (a) Geometrical design of the proposed unit cell, (b) Simulation of the unit cell using Floquet port boundary conditions in Ansys HFSS, and (c) Equivalent circuit of the proposed unit cell.

resonator [25]. This concept of a unit cell was originally introduced in [26] and [27]. The schematic diagram for the proposed unit cell is shown in Fig. 6(c). A PIN diode is placed in the middle gap of the improved ELC along the *x*-axis. The upper microstrip line is represented by inductors L_1 and L_2, while the lower microstrip line is represented by inductors L_3 and L_4. A microstrip line with an inductance L_5 illustrates the coupling between upper and lower microstrip lines, and the equivalent circuit of the PIN diode is characterized by R_1, L_6, and C_3. Furthermore, C_1 and C_2 represents capacitance between the microstrip lines. The ELC resonators have proven effective in realizing tunable, switchable, and multiband metamaterial devices [28]. Additionally, ELC resonators find common applications in various fields such as radar [29], radio frequency (RF) circuits [30], wireless power transfer systems [31], and planar differential sensors [32].

Each unit cell has a single PIN diode integrated at its center along the *x*-axis, allowing for the control of individual unit cell activation or deactivation. The unit cell utilizes the Skyworks SMP1340-079LF series PIN diodes [33], chosen for their high reliability, cost-effectiveness, and compatibility with low-control voltage switches. In the proposed unit

cell, digital representations of 1 and 0 denote the active and inactive states of the PIN diodes, respectively. When switched on, the diode presents a resistance (R) of 1 Ω and an inductance (L) of 0.7 nH. Conversely, in the off state, it exhibits a resistance of 10 kΩ, an inductance of 0.7 nH, and a capacitance (C) of 0.21 pF.

Fig. 7 illustrates the unit cell properties in terms of magnitude and phase for both the on and off operating states of the PIN diodes. At a center frequency of 3.5 GHz the unit cell demonstrates distinct transmission characteristics. In the on state of the diode, there is no transmission, indicated by a magnitude of 0.12. Conversely, when the diode is switched off, significant transmission occurs, with a magnitude of 0.99. The phase difference between these two states is found to be 25°.
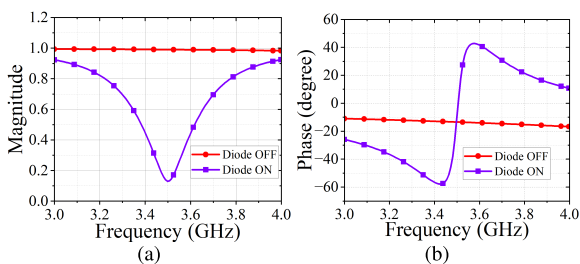

FIGURE 7. Transmission characteristics of the unit cell (a) Magnitude and (b) Phase.

The behavior of a material is significantly influenced by its electromagnetic characteristics, including permittivity (ϵ), permeability (μ), and conductivity. An analysis of these unit cell properties has been conducted at 3.5 GHz. The values for permittivity and permeability are obtained by extracting data from the full-wave simulator HFSS. Accurate complex curves for the permittivity and permeability of the metamaterial can be obtained by analyzing the unit cell transmission S-parameter (S_{21}) and reflection S-parameter (S_{11}). This data is processed using MATLAB script [34]. The unit cell exhibits unique characteristics with a negative permeability value and a positive permittivity value, indicating the presence of a single negative metamaterial property. The relationships between permittivity (ϵ), permeability (μ), refractive index (i), and impedance (η) can be mathematically expressed by equation 1 and equation 2. The presence of a negative refractive index and a positive impedance in Fig. 8 suggests that the unit cell exhibits characteristics of metamaterial behavior.

$$i = \frac{\mu}{\eta} \tag{1}$$

$$\eta = \sqrt{\frac{\mu}{\epsilon}} \tag{2}$$

The proposed TCMS incorporates a 9 × 9 array of unit cells. Fig. 9(a) presents top view of the 9 × 9 TCMS. The TCMS is characterized by dimensions measuring 144 mm in both length L and width W. It is positioned above the source antenna at a distance h_2. Notably, all the unit cells in column 5
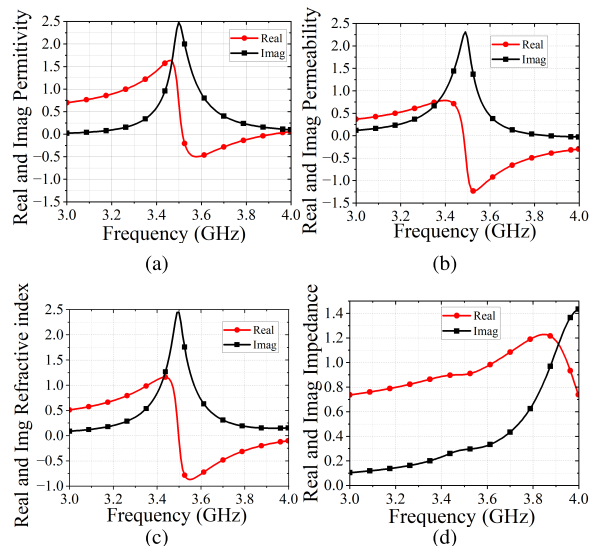

FIGURE 8. Extraction of unit cell parameters (a) Permittivity, (b) Permeability, (c) Refractive index, and (d) Impedance.

operate independently of the diode, ensuring a consistent emission of electromagnetic waves towards the upper region. When the diode is in the off state, the metasurface allows maximum transmission of electromagnetic waves. However, when the diode is switched on, majority of the waves are reflected back to the antenna resulting in secondary radiation. Increasing the number of unit cells with diodes in the off state compared to those in the on state focuses the radiation beam of the antenna toward unit cells with diodes off. The primary objective of using the TCMS is to control and direct main beam of the antenna in desired direction.

In the TCMS design, each PIN diode in the unit cell is regulated using an independent control system. To simplify the illustration, Fig. 9(b) shows only one row of bias lines, which mirrors the arrangement found in the other rows. A thin metal line directly connects the unit cell to the positive voltage of the DC line, while the negative voltage is routed through lines located at the substrates rear using metal vias. To minimize the impact of DC path on the microwave signal, the bias lines are kept narrow, with a width of 0.2 mm, matching the diameter of metal vias. During analysis it is noted that certain electric fields pass through the biasing lines. To address this issue, 13 nH surface-mounted RF choke inductors LQW03AW13NJ00D are employed within the biasing lines to mitigate the impact of RF currents [35]. Moreover, to block microwave signals in the DC paths, the bias lines are connected at the corner of each individual unit cell.

The separation between wideband cross-slot antenna and the TCMS is determined by equation 3, where λ_g represents guided wavelength at center frequency of 3.5 GHz and L_{eff} is effective length of the antenna [21]. By theoretical calculation, the effective length L_{eff} and guided wavelength λ_g of the wideband source antenna are 19.16 mm and 38.33 mm, respectively. By utilizing the values of L_{eff} and λ_g,
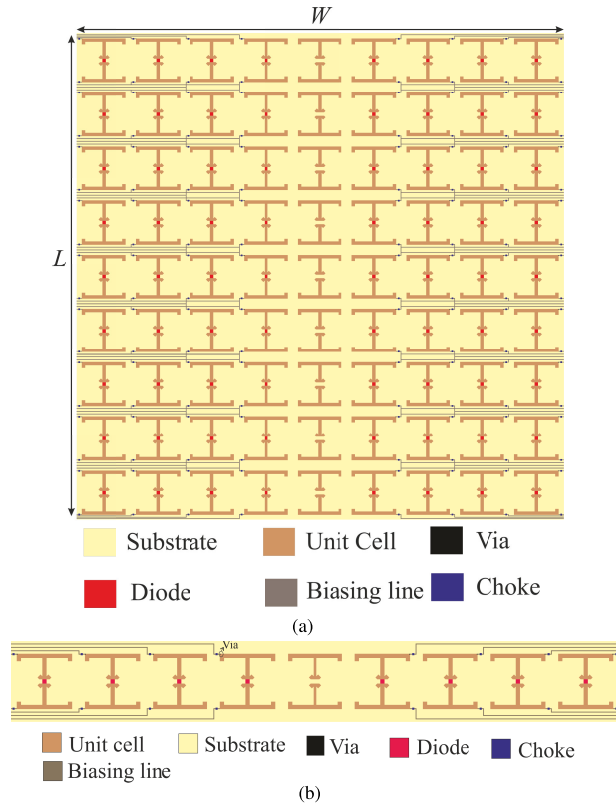
FIGURE 9. (a) Top view of 9 × 9 TCMS and (b) Top view of 1 × 9 TCMS.

it is found that the distance separating the cross-slot antenna and TCMS is 8.0020 mm, which can be approximated as $h_2 = 8$ mm. This configuration ensures optimal functionality of the TCMS and its ability to manipulate electromagnetic waves.

$$h_2 \leq 0.62 \sqrt{\frac{L_{eff}^3}{\lambda_g}} \tag{3}$$

D. CONTROL CIRCUIT

A simple and effective control circuit is designed to regulate ON/OFF states of PIN diodes on TCMS. Fig. 10 shows top and bottom view of the control circuit board. It consists of eight channels, with each channel connected to each column of unit cells in TCMS, except for the center column due to the absence of PIN diodes. This setup allows for the activation and deactivation of PIN diodes as needed. A lithium-ion battery powers the input supply to the control circuit through an XT-60 connector. The input power is regulated to 5 V DC using a voltage regulator IC 7805. The regulated 5 V output is then supplied to a microcontroller N76E003AT20 and a current limit circuit with an LM317 regulator. The output current of the current limit circuit can be adjusted by using PCB jumpers (JP1 to JP4) to select different current limits as needed. The control circuits output comprises a PNP driver transistor and a P-channel MOSFET. Applying a high voltage to the base of driver transistor causes it to pull down the gate of P-channel MOSFET to the ground, enabling the MOSFET to regulate

the output. The control circuit additionally features eight tactile switches, each accompanied by a suitable pull-up resistor, designed to detect their activation when pressed. LEDs are incorporated into the output of each channel; thus, when a specific channel is activated, its corresponding LED lights up, offering a visual representation of the operational status of each channel. Control circuits provide numerous advantages, including automation, precision, safety, energy efficiency, remote monitoring, flexibility, fault diagnosis, and easy integration.
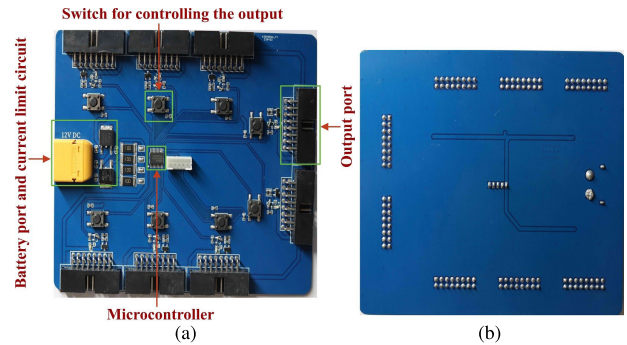

FIGURE 10. Fabricated prototype of the control circuit board (a) Top view and (b) Bottom view.

III. WORKING PRINCIPLE

This section focuses on operational principles of the proposed antenna. When a unit cell is configured as element 0, it signifies that the diode is in an off state. Conversely, when a unit cell is configured as element 1, it indicates that the diode is in the on state. Transmission capabilities of element 0 enable it to effectively transmit x-polarized waves, while element 1 has a relatively weaker ability to transmit such waves. Manipulating the coding sequences of the TCMS allows beam steering and beamwidth reconfigurability. To initiate this, it is necessary to configure all elements in the fifth column, positioned at the center, as element 0. This configuration facilitates the flow of electromagnetic energy along positive z-direction. Additionally, PIN diodes switching states in the same column are identical. Table 1 summarizes operating states of the proposed antenna.

TABLE 1. Operating states of the proposed antenna.

State	1	2	3	4	5	6	7	8	9	Operation
State 1	0	0	0	0	0	0	0	0	0	
State 2	0	1	0	0	0	0	0	1	0	
State 3	1	0	0	0	0	0	0	0	1	Beamwidth
State 4	1	1	0	0	0	0	0	1	1	reconfigurability
State 5	1	1	1	0	0	0	1	1	1	
State 6	1	1	1	1	0	1	1	1	1	
State 7	1	1	1	1	0	0	0	1	1	
State 8	1	1	1	1	0	0	0	0	1	
State 9	1	1	1	1	0	0	0	0	0	Beam steering
State 10	1	1	0	0	0	1	1	1	1	
State 11	1	0	0	0	0	1	1	1	1	
State 12	0	0	0	0	0	1	1	1	1	

Modifying coding sequences of the TCMS specified in Table 1 enables the reconfiguration of beamwidth, extending

the range of operating states from state 1 to state 6, thus offering flexibility in controlling the beam spread. An equal number of elements 0 and 1 positioned on both sides of the y-axis cause the primary beam to align toward the broadside. The simulated reflection characteristics for operating states from state 1 to state 6 are shown in Fig. 11(a). The overall −10 dB impedance bandwidth ranges from 3.09 to 3.70 GHz (17.96%). Normalized simulated radiation patterns for beamwidth reconfigurable operating states are illustrated in Fig. 12. The 3-dB beamwidth for state 1, state 2, state 3, state 4, state 5, and state 6 is 107°, 140°, 72°, 70°, 60°, and 64° respectively. The peak gain is found to be in the range from 5.38 to 9.08 dBi. From the simulated results, it can be concluded that state 2 shows a wide beam and state 5 demonstrates a narrow beam.
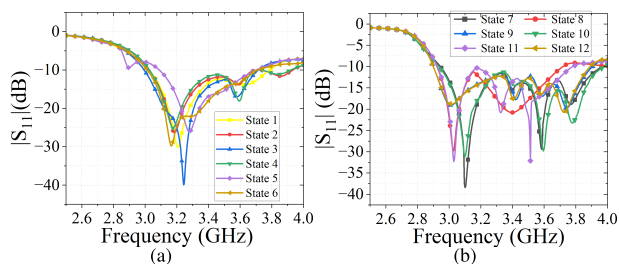

FIGURE 11. Simulated reflection characteristics of the proposed antenna (a) State 1 to state 6 and (b) State 7 to state 12.
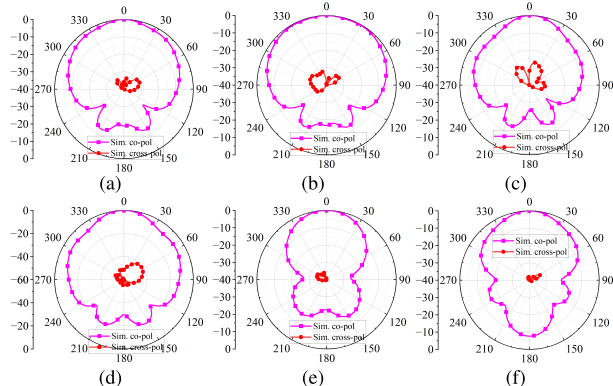
FIGURE 12. Normalized simulated radiation pattern at an operating frequency of 3.5 GHz in the yz-plane (a) State 1, (b) State 2, (c) State 3, (d) State 4, (e) State 5, and (f) State 6.

The beam steering in the yz-plane is achieved by using the coding sequences from state 7 to state 12. To steer the beam in $+\theta$ direction, there should be a higher frequency of element 0 occurrences on the right side than on the left, and vice versa for beam steering in the $-\theta$ direction. The combined −10 dB impedance bandwidth across all states of beam steering spans from 2.9 to 3.71 GHz (24.54%), as illustrated in Fig. 11(b). Normalized simulated radiation pattern for beam steering operating states are depicted in Fig. 13. As indicated in Table 1, the electric field density increases notably from state 7 to state 9 in columns six through nine, in contrast to the first four columns. Consequently, the main beam achieves maximum amplitude when oriented at a positive angle in the

yz-plane. The beam steering angles in state 7, state 8, and state 9 are +37°, +53°, and +57°, respectively. Conversely, from state 10 to state 12, the electric field density in the first four columns is significantly higher than in the sixth through ninth columns. The beam steering angles in state 10, state 11, and state 12 are −36°, −55°, and −57°, respectively. The peak gains for state 7, state 8, state 9, state 10, state 11, and state 12 are 8.46 dBi, 6.71 dBi, 7.49 dBi, 8.47 dBi, 6.26 dBi, and 7.76 dBi, respectively.
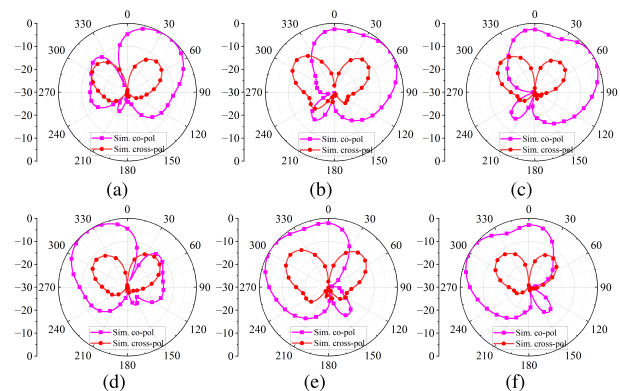

FIGURE 13. Normalized simulated radiation pattern at an operating frequency of 3.5 GHz in the yz-plane (a) State 7, (b) State 8, (c) State 9, (d) State 10, (e) State 11, and (f) State 12.

IV. SIMULATED AND MEASURED RESULTS

The proposed wideband beam steering and beamwidth reconfigurable antenna is developed using FR4 substrate. Fig. 14 displays photographs of the fabricated antennas. Performance of the developed antenna is experimentally analyzed using a vector network analyzer (VNA). The antennas radiation characteristics are evaluated in a far-field anechoic chamber. The novel control circuit board manages activation and deactivation of the PIN diodes. The fabricated antenna has been tested mainly in six states across frequencies 3.3 GHz, 3.5 GHz, and 3.7 GHz. The measurements are performed for beamwidth reconfigurable conditions state 2 and state 5 and beam steering conditions state 7, state 9, state 10, and state 12.

A. REFLECTION CHARACTERISTICS

This section presents detailed simulated and measured reflection characteristics of the proposed antenna. The simulated and measured impedance bandwidth for state 2 ranges from 3.02 to 3.93 GHz and 3.10 to 3.77 GHz, respectively, as depicted in Fig. 15(a). For state 5, the simulated and measured impedance bandwidth is from 3.09 to 3.70 GHz and 3.14 to 3.70 GHz, respectively, as displayed in Fig. 15(b). The overlapped impedance bandwidth in state 2 and state 5 is 3.10 to 3.77 GHz (19.5%) and 3.14 to 3.70 GHz (16.37%), respectively. The simulated impedance bandwidth of state 7 and state 9 is 2.94 to 3.97 GHz and 2.90 to 3.90 GHz, respectively. The measured impedance bandwidth ranges from 2.91 to 3.88 GHz and 2.86 to 3.83 GHz, respectively. The overlapped impedance bandwidth of state 7 and state 9 is 2.94 to 3.90 GHz (28.07%) and 2.91 to 3.83 GHz (27.29%),
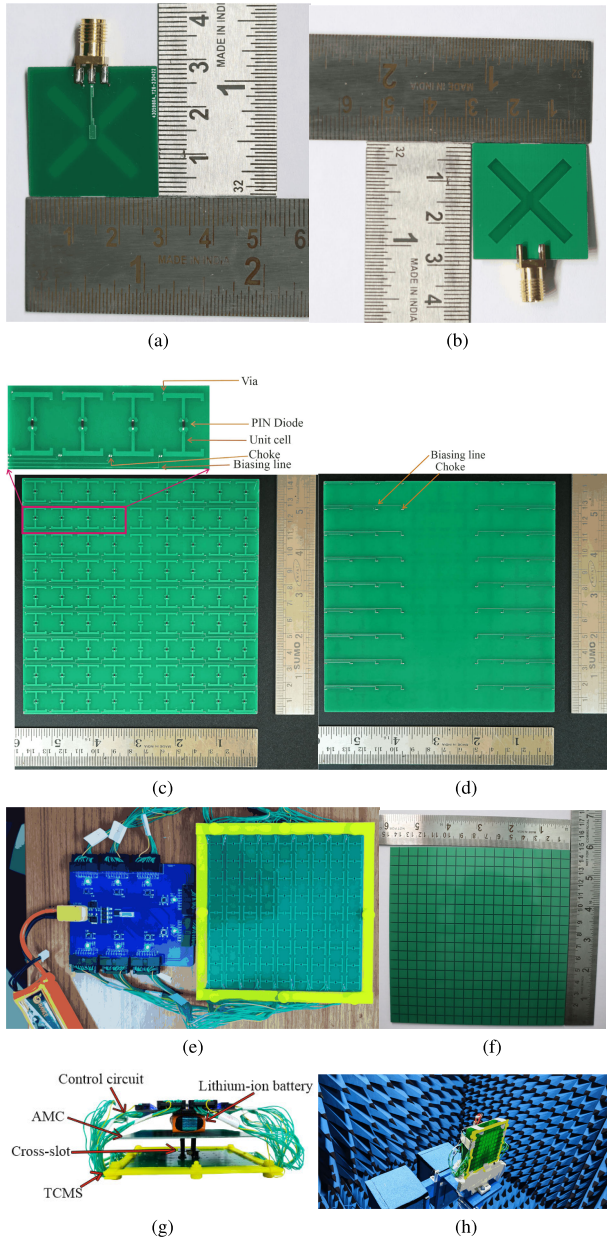
FIGURE 14. Photographs of (a) Top view of cross-slot antenna, (b) Bottom view of cross-slot antenna, (c) Top view of TCMS, (d) Bottom view of TCMS, (e) TCMS with control circuit, (f) AMC, (g) Side view of the antenna, and (h) Testing setup used in the anechoic chamber.

respectively, as illustrated in Fig. 15(c). Moving on to state 10 and state 12, the simulated impedance bandwidths are 2.94 to 3.98 GHz and 2.90 to 3.89 GHz, respectively. The measured impedance bandwidth for state 10 and state 12 is 2.86 to 3.87 GHz and 2.86 to 3.83 GHz, respectively. The overlapped impedance bandwidth for state 10 and state 12 is 2.94 to 3.89 GHz (27.85%) and 2.86 to 3.83 GHz (29.04%), respectively, as shown in Fig. 15(d).

B. RADIATION CHARACTERISTICS

This section presents detailed simulated and measured radiation characteristics of the proposed antenna in beamwidth
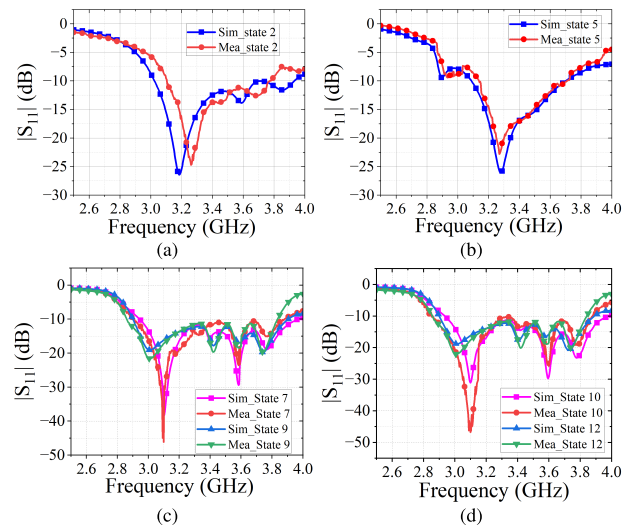
FIGURE 15. Simulated and measured reflection characteristics of the proposed antenna in different operating states (a) State 2, (b) State 5, (c) State 7 and state 9, and (d) State 10 and state 12.

reconfigurable and beam steering operating states at frequencies 3.3 GHz, 3.5 GHz, and 3.7 GHz. Fig. 16 shows normalized simulated and measured radiation patterns for state 2 and state 5. In state 2, the simulated 3-dB beamwidths are 108°, 140°, and 61°, whereas the measured 3-dB beamwidths are 86°, 102°, and 60°. For state 5, the simulated results show 3-dB beamwidths of 65°, 60°, and 61°, while the measured 3-dB beamwidths are 58°, 52°, and 54°. It can be concluded that the overall beamwidth of the antenna can be controlled to achieve both wide and narrow beams. For state 2, the simulated and measured peak gain ranges from 5.26 to 6.49 dBi and from 5.08 to 5.60 dBi, respectively. In state 5, the simulated peak gain varies from 6.25 to 7.5 dBi, whereas the measured gain fluctuates between 6.21 dBi and 6.62 dBi. The simulated radiation efficiency is 84.73% for state 2 and 85.90% for state 5.
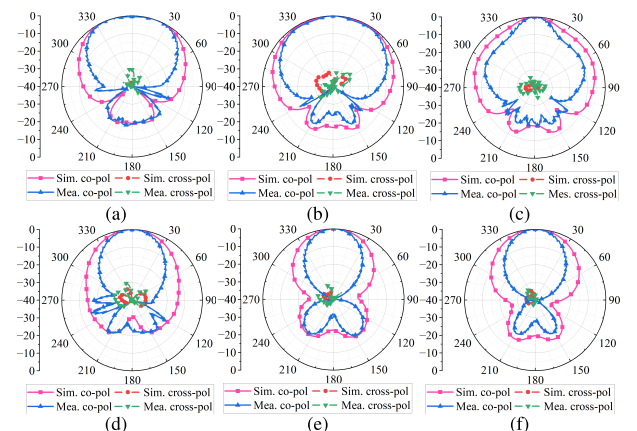
FIGURE 16. Normalized simulated and measured radiation pattern in the *yz*-plane for (a) State 2 (3.3 GHz), (b) State 2 (3.5 GHz), (c) State 2 (3.7 GHz), (d) State 5 (3.3 GHz), (e) State 5 (3.5 GHz), and (f) State 5 (3.7 GHz).

Fig. 17 and Fig. 18 displays the normalized simulated and measured radiation patterns for the beam steering operating

states. State 7 and state 9 exhibit beam steering in the $+\theta$ direction, while state 10 and state 12 demonstrate beam steering in the $-\theta$ direction. In state 7, main beam of the antenna is directed at $+35°$, $+37°$, and $+25°$, while the measured beam is directed at $+32°$, $+34°$, and $+27°$. For state 9, the simulated main lobe direction is $+54°$, $+57°$, and $+56°$, whereas the measured angles are $+53°$, $+56°$, and $+57°$. In state 10, the simulated main lobe direction is $-34°$, $-36°$, and $-25°$, while the measured angles are $-32°$, $-34°$, and $-26°$. In state 12, the simulated main lobe direction is $-52°$, $-57°$, and $-56°$, and the measured angles are $-54°$, $-56°$, and $-58°$.
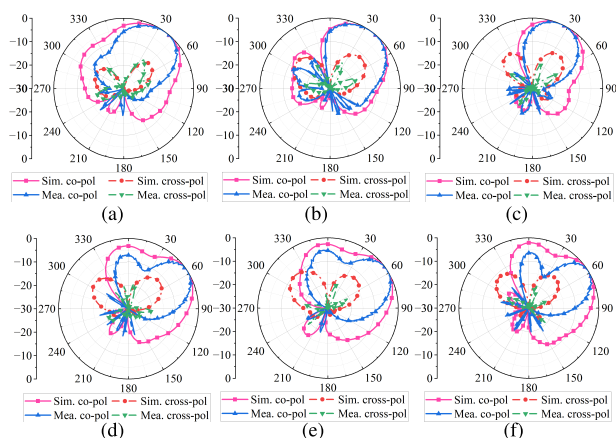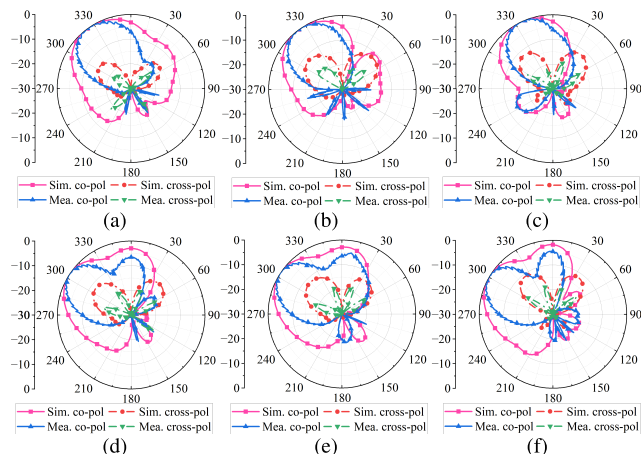

FIGURE 17. Normalized simulated and measured radiation pattern in the yz-plane for (a) State 7 (3.3 GHz), (b) State 7 (3.5 GHz), (c) State 7 (3.7 GHz), (d) State 9 (3.3 GHz), (e) State 9 (3.5 GHz), and (f) State 9 (3.7 GHz).


FIGURE 18. Normalized simulated and measured radiation pattern in the yz-plane for (a) State 10 (3.3 GHz), (b) State 10 (3.5 GHz), (c) State 10 (3.7 GHz), (d) State 12 (3.3 GHz), (e) State 12 (3.5 GHz), and (f) State 12 (3.7 GHz).

Fig. 19 displays main beam direction and variations in peak gain across the frequency range from 3.3 to 3.7 GHz. It is observed that the primary beam direction exhibits minimal variation across the frequency range from 3.3 to 3.7 GHz, as illustrated in Fig. 19(a). State 7 exhibits a simulated peak gain ranging from 6.42 dBi to 8.46 dBi, while the measured gain ranges from 5.62 dBi to 6.26 dBi, as shown in Fig. 19(b).

For state 9, the simulated peak gain fluctuates from 8.04 dBi to 7.49 dBi, with the measured gain varies from 7.24 dBi to 6.68 dBi. State 10 demonstrates a simulated peak gain ranging from 6.64 dBi to 8.47 dBi, while the measured gain spans from 6.24 dBi to 7.58 dBi. In state 12, the simulated peak gain ranges from 7.75 dBi to 7.76 dBi and the measured gain varies from 7.24 dBi to 6.42 dBi. It can be noted that the proposed antenna maintains a consistent gain within the range of 5.62 dBi to 8.47 dBi across different states and frequencies. The simulated radiation efficiency is 75.83% for state 7, 72.40% for state 9, 75.92% for state 10, and 71.54% for state 12. The cross-polarization levels consistently remain below -15 dB throughout the entire operating frequency range. Slight variations in both simulated and measured gains occur due to losses incurred by PIN diodes and biasing lines. Fig. 20 illustrates 3-D polar radiation patterns of the proposed antenna in different operating states at the center frequency of 3.5 GHz.
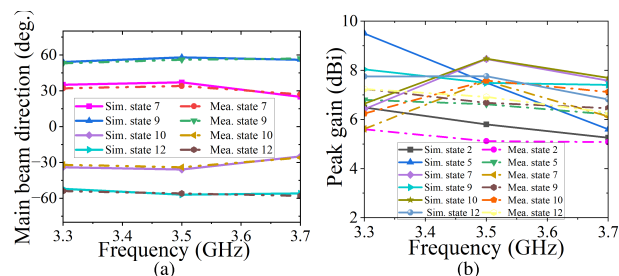
FIGURE 19. Simulated and measured results across the frequency range from 3.3 to 3.7 GHz (a) Main beam direction of beam steering states and (b) Peak gain of beam steering and beamwidth reconfigurable states.
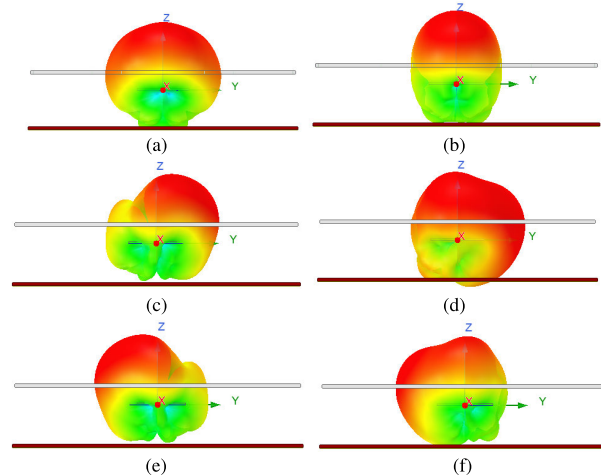
FIGURE 20. 3-D polar radiation pattern at 3.5 GHz in (a) State 2, (b) State 5, (c) State 7, (d) State 9, (e) State 10, and (f) State 12.

C. PERFORMANCE COMPARISON

Table 2 provides a performance comparison between the proposed wideband pattern reconfigurable antenna and prior reported works in terms of -10 dB impedance bandwidth, beam steering range, 3-dB beamwidth, peak gain, overall

TABLE 2. Performance comparison of the proposed beam steering and beamwidth reconfigurable antenna with the earlier reported works.

Ref.	Antenna type	Operating frequency (GHz)	−10 dB bandwidth (%)	Beam steering (degree)	3-dB beamwidth (degree)	Peak gain (dBi)	Size (λ_0^3) (mm^3)	Switches (number)
[12]	Parasitic pixel	5	4	±40	40 (E-plane), 100 (H-plane) 100 (D-plane)	8	1×1×0.18	PIN (6)
[13]	Tunable parasitic	2.45	1.63	10.8 (E-plane) 40 (H-plane) 32.4 (D-plane)	65 to 152 (E-plane) 64 to 116 (H-plane)	3.78	1.143×1.143×0.013	varactor (8)
[14]	Tunable parasitic	1.4	6.40	±20 (H-plane)	60 to 130 (H-plane)	8.8	1.49×0.47×NA	varactor (2)
[15]	Parasitic	3.5	5.56	−17, 14	49, 105	7	1.16×1.16×0.079	PIN (8)
[16]	PRS	2	3	±10 (H-plane)	18.7 to 22.4 (H-plane)	14.7	NA	varactor (100)
[17]	Antenna with metal walls	3.7	10.8	−51, 54 (E-plane) −20, 20 (H-plane)	narrow wide	6	0.53×0.53×0.235	PIN (2)
[18]	Circular patch	2.08	1	four steerable beams	82 to 190 (Elevation)	3	Radius 30 mm	-
[19]	Metasurface	3.33	NA	−49 to 50 (E-plane)	48, 37 (E-plane)	18	4.26×0.335×NA	varactor (90)
[20]	Metasurface	2.4	> 20	−39, 0, 36 (E-plane)	111 to 32 (E-plane)	14.5	1.92×1.6×0.296	two low noise amplifiers
[21]	Metasurface	3.9	0.7	±85	wide beam (130) narrow beam (53)	5.73	1.46×1.46×0.146	PIN (42)
Proposed	Cross-slot with metasurface	3.5	17.96	± 57	wide beam (140) narrow beam (60)	8.47	1.7×1.7×0.39	PIN (72)

NA: Not available

size, and number of switches used. It is observed that the antenna designs reported in [12], [14], [16], [18], and [19] has limitations in terms of impedance bandwidth, beam steering, and beamwidth reconfigurability. The pattern reconfigurable antenna designs presented in [13] and [18] demonstrate good beamwidth reconfigurability, however, they are limited by lower bandwidth and gain. On the other hand, the antenna design presented in [20] exhibits a higher bandwidth, but it is restricted to three beam steering states. Additionally, in [21] wide angle beam steering is achieved with narrow beam and wide beam operating modes. However, this antenna is associated with a narrow operating bandwidth of 0.7%. The proposed antenna achieves independent beam steering from −57° to +57° and beamwidth reconfigurability with wide beam and narrow beam operating modes. This antenna achieves a wide bandwidth of 17.96%, which is higher as compared with the previously reported works.

V. CONCLUSION

This paper presents a wideband pattern reconfigurable antenna capable of independent beam steering and beamwidth reconfigurability. Pattern reconfiguration is achieved across a broad frequency range from 3.09 to 3.70 GHz (17.96%), making it suitable for 5G applications. The wideband characteristics are achieved through the utilization of a cross-slot antenna. By integrating an AMC with a coding metasurface, the antenna achieves a high gain

of 8.47 dBi along with pattern reconfiguration capabilities. One notable advantage of the proposed antenna is its ability to achieve both beam steering and beamwidth reconfiguration within a single antenna structure, while maintaining wideband characteristics. The antenna allows for beam steering ranging from −57° to +57°, with minimal gain variation across the entire beam steering range. Additionally, the antenna offers beamwidth variability through narrow and wide beam operating modes.

REFERENCES

[1] J. T. Bernhard, *Reconfigurable Antennas*. San Rafael, CA, USA: Morgan & Claypool, 2007.

[2] K. S. Satish and J.-C. S. Chieh, *MultiFunctional Antennas and Arrays for Wireless Communication Systems*. Hoboken, NJ, USA: Wiley, 2021.

[3] A. Khidre, F. Yang, and A. Z. Elsherbeni, "Circularly polarized beam-scanning microstrip antenna using a reconfigurable parasitic patch of tunable electrical size," *IEEE Trans. Antennas Propag.*, vol. 63, no. 7, pp. 2858–2866, Jul. 2015.

[4] V. V. Khairnar, B. V. Kadam, C. K. Ramesha, and L. J. Gudino, "A reconfigurable parasitic antenna with continuous beam scanning capability in H-plane," *AEU Int. J. Electron. Commun.*, vol. 88, pp. 78–86, May 2018.

[5] L.-Y. Ji, Y. J. Guo, P.-Y. Qin, S.-X. Gong, and R. Mittra, "A reconfigurable partially reflective surface (PRS) antenna for beam steering," *IEEE Trans. Antennas Propag.*, vol. 63, no. 6, pp. 2387–2395, Jun. 2015.

[6] Z. Li, E. Ahmed, A. M. Eltawil, and B. A. Cetiner, "A beam-steering reconfigurable antenna for WLAN applications," *IEEE Trans. Antennas Propag.*, vol. 63, no. 1, pp. 24–32, Jan. 2015.

[7] P. Lotfi, S. Soltani, and R. D. Murch, "Broadside beam-steerable planar parasitic pixel patch antenna," *IEEE Trans. Antennas Propag.*, vol. 64, no. 10, pp. 4519–4524, Oct. 2016.

[8] S.-L. Chen, P.-Y. Qin, W. Lin, and Y. J. Guo, "Pattern-reconfigurable antenna with five switchable beams in elevation plane," *IEEE Antennas Wireless Propag. Lett.*, vol. 17, pp. 454–457, 2018.

[9] Y. Li and K.-M. Luk, "A linearly polarized magnetoelectric dipole with wide H-plane beamwidth," *IEEE Trans. Antennas Propag.*, vol. 62, no. 4, pp. 1830–1836, Apr. 2014.

[10] B. Feng, Y. Tu, K. L. Chung, and Q. Zeng, "A beamwidth reconfigurable antenna array with triple dual-polarized magneto-electric dipole elements," *IEEE Access*, vol. 6, pp. 36083–36091, 2018.

[11] Y. Shi, Y. Cai, J. Yang, and L. Li, "A magnetoelectric dipole antenna with beamwidth reconfiguration," *IEEE Antennas Wireless Propag. Lett.*, vol. 18, pp. 621–625, 2019.

[12] Md. A. Towfiq, I. Bahceci, S. Blanch, J. Romeu, L. Jofre, and B. A. Cetiner, "A reconfigurable antenna with beam steering and beamwidth variability for wireless communications," *IEEE Trans. Antennas Propag.*, vol. 66, no. 10, pp. 5052–5063, Oct. 2018.

[13] V. V. Khairnar, B. V. Kadam, C. K. Ramesha, and L. J. Gudino, "A reconfigurable microstrip cross parasitic antenna with complete azimuthal beam scanning and tunable beamwidth," *Int. J. RF Microw. Comput.-Aided Eng.*, vol. 29, no. 1, Jan. 2019, Art. no. e21472.

[14] J. Wang, J. Yin, H. Wang, C. Yu, and W. Hong, "Wideband U-slot patch antenna with reconfigurable radiation pattern," in *Proc. 11th Eur. Conf. Antennas Propag. (EUCAP)*, Mar. 2017, pp. 611–615.

[15] W.-Q. Deng, X.-S. Yang, C.-S. Shen, J. Zhao, and B.-Z. Wang, "A dual-polarized pattern reconfigurable Yagi patch antenna for microbase stations," *IEEE Trans. Antennas Propag.*, vol. 65, no. 10, pp. 5095–5102, Oct. 2017.

[16] T. Debogovic and J. Perruisseau-Carrier, "Array-fed partially reflective surface antenna with independent scanning and beamwidth dynamic control," *IEEE Trans. Antennas Propag.*, vol. 62, no. 1, pp. 446–449, Jan. 2014.

[17] G. Yang, J. Li, D. Wei, S.-G. Zhou, and R. Xu, "Pattern reconfigurable microstrip antenna with multidirectional beam for wireless communication," *IEEE Trans. Antennas Propag.*, vol. 67, no. 3, pp. 1910–1915, Mar. 2019.

[18] Z. Zhang, S. Cao, and J. Wang, "Azimuth-pattern reconfigurable planar antenna design using characteristic mode analysis," *IEEE Access*, vol. 9, pp. 60043–60051, 2021.

[19] S. Lim, C. Caloz, and T. Itoh, "Metamaterial-based electronically controlled transmission-line structure as a novel leaky-wave antenna with tunable radiation angle and beamwidth," *IEEE Trans. Microw. Theory Techn.*, vol. 53, no. 1, pp. 161–173, Jan. 2005.

[20] T. Liang, Z. Wang, and Y. Dong, "A beamwidth and steering reconfigurable active integrated metasurface antenna for dynamic radiation control," *IEEE Trans. Antennas Propag.*, vol. 70, no. 10, pp. 9006–9016, Oct. 2022.

[21] L. L. Sheng, W. P. Cao, L. R. Mei, and X. H. Yu, "A novel low-cost beam-controlling antenna based on digital coding metasurface," *Int. J. RF Microw. Comput.-Aided Eng.*, vol. 32, no. 6, Jun. 2022, Art. no. e23152.

[22] T. J. Cui, M. Q. Qi, X. Wan, J. Zhao, and Q. Cheng, "Coding metamaterials, digital metamaterials and programmable metamaterials," *Light, Sci. Appl.*, vol. 3, no. 10, p. e218, Oct. 2014.

[23] *High Frequency Structure Simulator (HFSS), Version 21*, Ansys, Canonsburg, PA, USA, 2006.

[24] Y. F. Cao and X. Y. Zhang, "A wideband beam-steerable slot antenna using artificial magnetic conductors with simple structure," *IEEE Trans. Antennas Propag.*, vol. 66, no. 4, pp. 1685–1694, Apr. 2018.

[25] D. Li, Z. Szabo, X. Qing, E.-P. Li, and Z. N. Chen, "A high gain antenna with an optimized metamaterial inspired superstrate," *IEEE Trans. Antennas Propag.*, vol. 60, no. 12, pp. 6018–6023, Dec. 2012.

[26] D. Schurig, J. J. Mock, and D. R. Smith, "Electric-field-coupled resonators for negative permittivity metamaterials," *Appl. Phys. Lett.*, vol. 88, no. 4, Jan. 2006, Art. no. 041109.

[27] R. Liu, A. Degiron, J. J. Mock, and D. R. Smith, "Negative index material composed of electric and magnetic resonators," *Appl. Phys. Lett.*, vol. 90, no. 26, Jun. 2007, Art. no. 263504.

[28] H.-M. Lee and H.-S. Lee, "Resonant mode behavior of lumped-resistor-loaded electric-inductive-capacitive resonator and its absorber application," *AIP Adv.*, vol. 3, no. 5, May 2013, Art. no. 052117.

[29] S. Bhattacharyya, S. Ghosh, and K. V. Srivastava, "Bandwidth-enhanced metamaterial absorber using electric field–driven lc resonator for airborne radar applications," *Microw. Opt. Technol. Lett.*, vol. 55, no. 9, pp. 2131–2137, Sep. 2013.

[30] W. Withayachumnankul, C. Fumeaux, and D. Abbott, "Compact electric-LC resonators for metamaterials," *Opt. Exp.*, vol. 18, no. 25, p. 25912, 2010.

[31] H. Ojukwu, B.-C. Seet, and S. U. Rehman, "Metasurface-aided wireless power transfer and energy harvesting for future wireless networks," *IEEE Access*, vol. 10, pp. 52431–52450, 2022.

[32] P. K. Varshney, A. Kapoor, and M. J. Akhtar, "Highly sensitive ELC resonator based differential sensor," *IEEE Trans. Instrum. Meas.*, vol. 70, pp. 1–10, 2021.

[33] *Data Sheet of SMP1340 Series: Fast Switching-Speed, Low Capacitance, Plastic-Packaged PIN Diodes*, Skyworks Solutions, Irvine, CA, USA.

[34] A. B. Numan and M. S. Sharawi, "Extraction of material parameters for metamaterials using a full-wave simulator [education column]," *IEEE Antennas Propag. Mag.*, vol. 55, no. 5, pp. 202–211, Oct. 2013.

[35] *Data Sheet of LQW03AW13NJ00D: Wire Wound RF Inductor*, Murata, Kyoto, Japan.

GANDHAM V. VINOD (Student Member, IEEE) received the B.E. degree in electronics and communication engineering and the M.E. degree in VLSI-design from Anna University, Chennai, Tamil Nadu, India, in 2006 and 2010, respectively. He is currently an Internal Full-Time Research Scholar with the School of Electronics Engineering (SENSE), VIT-AP University, Amaravati, Andhra Pradesh, India. His research interests include the design of pattern reconfigurable antennas using metasurface, CP beam steering using metasurface, and transmissive and reflective metasurface for 5G and beyond applications.

VIKAS V. KHAIRNAR (Member, IEEE) received the B.E. degree in electronics and telecommunication engineering from Savitribai Phule Pune University, India, in 2009, the M.E. degree in communication engineering from Dr. BAMU University, India, in 2013, and the Ph.D. degree from BITS Pilani, India, in 2020. He is currently working as an Assistant Professor with the School of Electronics Engineering (SENSE), VIT-AP University, Amaravati, Andhra Pradesh, India. His research interests include the design of reconfigurable antennas, antenna arrays, and metasurface inspired antennas.

• • •